NANO LETTERS

pubs.acs.org/NanoLett Letter

Vacancy Defects in 2D Ferroelectric In_2Se_3 and the Conductivity Modulation by Polarization−Defect Coupling

Ming-Yu Ma, Dan Wang,* Yu-Ting Huang,* Dong Han, Nian-Ke Chen,* Hong-Bo Sun, Shengbai Zhang, and Xian-Bin Li*

Cite This: https://doi.org/10.1021/acs.nanolett.4c05165 Read Online

ACCESS | Metrics & More | Article Recommendations | Supporting Information

ABSTRACT: α-In_2Se_3 is a promising two-dimensional (2D) ferroelectric semiconductor with unique phase transition behaviors and intrinsic *n*-type conductivity. However, the origin of this conductivity and the impact of defects on the phase transition remain unclear. In this study, we employed the WLZ method to calculate vacancies' formation energy and ionization energy in monolayer α-In_2Se_3 and identified the defect-bound band edge states. Our results reveal a strong polarization−defect coupling effect, where the bottom-layer selenium vacancy drives intrinsic *n*-type conductivity in the sample with upward polarization while reversing the polarization-induced deep *p*-type defect. Furthermore, we demonstrate that a vacancy stabilizes the ferroelectric phase and reduces the phase transition rate to the paraelectric phase. Finally, we propose a defect-engineered ferroelectric field-effect transistor model that controls the resistance by leveraging the polarization−defect coupling effect. This work highlights the significant roles of vacancy defects in 2D α-In_2Se_3, offering strategies to design In_2Se_3 electronic devices at the nanoscale.

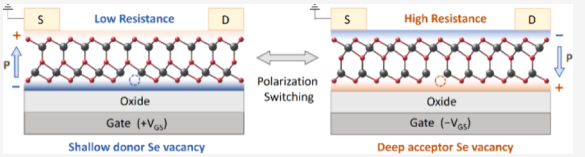

KEYWORDS: *Polarization−defect coupling, n-type monolayer α-In_2Se_3, Defect-engineered FeS-FET, WLZ method, First-principles calculations*

Ferroelectric materials, characterized by their retentive and switchable electric dipoles, are ideal candidates for building nonvolatile memory devices with low power consumption and ultrafast logic operations. These materials hold the potential to address the bottleneck arising from the separation of processing and storage units in traditional von Neumann computing architectures.[1,2] The utilization of two-dimensional (2D) ferroelectric materials significantly reduces device size, thus lowering the write or erase voltages required for polarization switching, making the realization of low-power memory devices feasible.[3−5] In 2017, Ding et al. first predicted that the 2D monolayer material In_2Se_3 exhibits at least two typical phases: the ferroelectric α and the paraelectric β.[6] The transition from α to β phase is driven by a highly coherent motion of shear phonon mode, which can reduce the potential barrier to 0.066 eV per unit cell.[6] α-In_2Se_3, with its asymmetric structure, could maintain stable ferroelectricity at the atomic scale, potentially breaking through the critical size limitations of traditional ferroelectric materials.[7] Additionally, it features high carrier mobility,[8] a strain-driven bandgap spanning the entire visible to near-infrared wavelength range,[9] and stable room-temperature in-plane and out-of-plane ferroelectricity within a single layer,[6] making it a strong candidate for widespread applications in ferroelectric tunnel junctions (FTJs),[10,11] ferroelectric field-effect transistors (FeFETs),[12,13] ferroelectric semiconductor field-effect transistors (FeS-FETs),[8,14,15] and storage and neuromorphic computing systems.[1,16,17]

In traditional FeFETs, the semiconductor channel and the ferroelectric gate are separated. The polarization of the ferroelectric α-In_2Se_3 regulates the carrier type and density in the semiconductor channel layer, offering high scalability and nondestructive readout associated with polarization switching. However, practical application is hindered by issues such as charge trapping and electrical breakdown.[12,13] In FeS-FETs, by exploiting the ferroelectricity and semiconductor properties of α-In_2Se_3, the polarization switching process can occur within the channel material itself rather than in the gate dielectric layer. This configuration potentially solves the issues of charge trapping and leakage current found in conventional FeFETs, offering a large memory window, high on/off ratio, long retention time, and substantial on-state current.[8,14,15]

α-In_2Se_3 consistently displays robust intrinsic *n*-type conductivity, as evidenced by numerous experiments.[18−21] Several studies have also concentrated on how defects influence the electronic properties of the material. In 2020, Hou et al. reported the displacement damage caused by neutron radiation, mainly examining the impact of indium vacancies.[22−24] Additionally, it was observed that a selenium

Received: October 17, 2024
Revised: February 16, 2025
Accepted: February 21, 2025

vacancy can also be generated through Ar^{2+} ion irradiation, enhancing the photodetection properties of the material.[25] In 2021, Tang et al. explored the electrical properties of five single-vacancy defects in 2D α-In_2Se_3, identifying appropriate donor and acceptor defects from the energy band diagrams related to these defects, but they did not quantify their ionization energies.[26] Although these studies have contributed to the development of 2D α-In_2Se_3, the origin of its intrinsic *n*-type conductivity, the identification, and the effect of defects on its phase transition remain unclear. Understanding these aspects is essential for the design and functionality of ferroelectric and electronic devices utilizing α-In_2Se_3.

In this work, we systematically evaluate the ionization energy (IE) using the WLZ method, exploring the origin of intrinsic *n*-type conductivity in 2D α-In_2Se_3 and the impact of vacancy defects on carriers and the phase transition. We also provide simulated scanning tunneling microscopy (STM) images to support future experimental identification of these defects. Building on the polarization-defect coupling, we propose a new design of a defect-engineered ferroelectric field-effect transistor with α-In_2Se_3 containing vacancy defects as the channel material. By adjustment of the gate voltage, the defect structures of α-In_2Se_3 change corresponding to different polarization directions, and then their resistance states would change accordingly. This work not only advances our understanding of the defect properties in 2D α-In_2Se_3 but also paves the way for developing nonvolatile electronic devices based on defect engineering in nano-ferroelectric materials.

We performed first-principles calculations based on density functional theory (DFT) within the Vienna Ab initio Simulation Package (VASP).[27,28] The Perdew–Burke–Ernzerhof functional (PBE) of the generalized gradient approximation (GGA) was selected.[29] The cutoff energy of the plane wave basis is 275 eV, and a 3 × 3 × 1 Monkhorst–Pack mesh grid is used for *k*-point sampling. The effect of spin polarization was taken into account in all of the calculations. The valence electrons of pseudopotentials[30] are indium (In, $4d^{10}5s^25p^1$) and selenium (Se, $4s^24p^4$). We calculated the formation energies and the ionization energies of five vacancies using eq S1 and eq S2 in the Supporting Information (SI) for lateral dimensions $L_X \times L_Y = 4 \times 4$, 5×5, and 6×6, with a vacuum thickness (L_Z) of 60 Å. The ionization energies were then extrapolated to infinite size using eq S3 in the SI to obtain the converged ionization energy according to the WLZ method.[31,32] STM scans were simulated with constant height mode, and the results were shown by VASPKIT.[33] For the molecular dynamics (MD) simulations, we chose the indium atomic pseudopotential with valence electrons of $5s^25p^1$ and a plane-wave basis with the cutoff energy of 250 eV. We performed the MD simulations using an NVT ensemble and a supercell containing 245 atoms.[34] The Brillouin zone was sampled with a single Γ point, and the MD time step was set to 1 fs. The energy barriers for domain wall motion were evaluated using the climbing image nudged elastic band (CI-NEB) method,[35] where electronic minimization was carried out with a tolerance of 10^{-6} eV, and ionic relaxation was performed with a force tolerance of 0.04 eV·Å^{-1} per ion.

Figure 1(a) shows the atomic structure of monolayer α-In_2Se_3, consisting of five atomic sublayers with alternating In and Se atoms. The calculated PBE bandgap of α-In_2Se_3 is 0.79 eV, consistent with the previous theoretical studies.[6] Given the diverse chemical environments of the five atomic sublayers, we

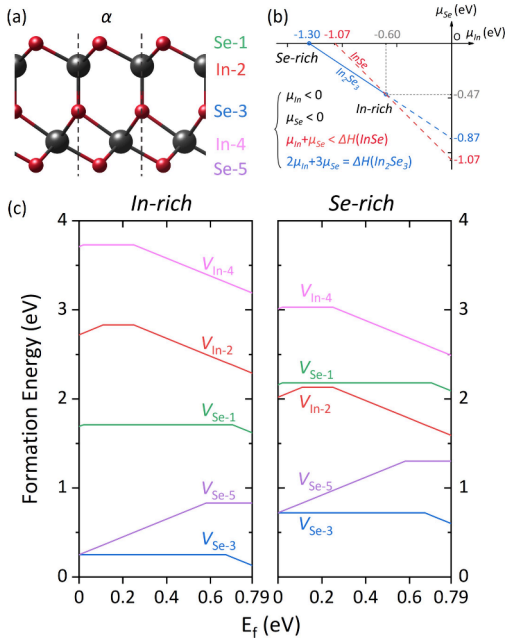

Figure 1. (a) Schematic atomic structure of 2D α phase In_2Se_3 and the name of the atom in each sublayer. (b) The ambient chemical potentials of the In and Se atoms must be carefully controlled to prevent the formation of a secondary phase (e.g., InSe) and to ensure the production of α-In_2Se_3. (c) Formation energies of various vacancy defects in α-In_2Se_3 under In-rich and Se-rich conditions.

explore five different types of vacancy defects. The formation of defects is closely related to the experimental conditions of growth or annealing, such as In-rich or Se-rich environments or conditions intermediate between these. Moreover, to prevent the formation of the popular secondary phase InSe,[36,37] it is crucial to ensure that the sum of the chemical potentials of In and Se in a 1:1 ratio is less than the formation energy of the InSe phase, i.e., $\mu_{In} + \mu_{Se} < \Delta H(InSe)$, as depicted in Figure 1(b). Similarly, the avoidance of elemental phases such as pure indium or selenium also necessitates that the relative chemical potentials of In and Se be less than zero. Ultimately, only the points along the solid blue line align with all of the requirements. The end points of this line correspond to In-rich and Se-rich extreme conditions, with the formation energies for five types of vacancy defects presented in Figure 1(c).

In the conventional case for the neutral state, it is evident that In vacancies have lower formation energies under Se-rich conditions, while Se vacancies show lower formation energies under In-rich conditions. This is expected because under Se-rich conditions the scarcity of In promotes the formation of In vacancies, whereas under In-rich conditions, the abundance of In favors the formation of Se vacancies. Among all studied defects, V_{Se-3} has the smallest neutral formation energy at 0.25 eV under In-rich conditions, indicating that the middle-layer Se atomic vacancy of α-In_2Se_3 forms readily. Conversely, the neutral formation energies for In vacancies exceed 2 eV even under Se-rich conditions, indicating that these vacancies are relatively difficult to form. One interesting point is that the formation energies of V_{Se-3} and V_{Se-5} remain low even under Se-rich condition, and this phenomenon of abnormally low Se vacancy formation energy can also be observed in other selenide research.[38] In our analysis of charged defects at the +1 and −1 charge states, we observe that V_{Se-3} and V_{Se-5} establish

https://doi.org/10.1021/acs.nanolett.4c05165
Nano Lett. XXXX, XXX, XXX−XXX

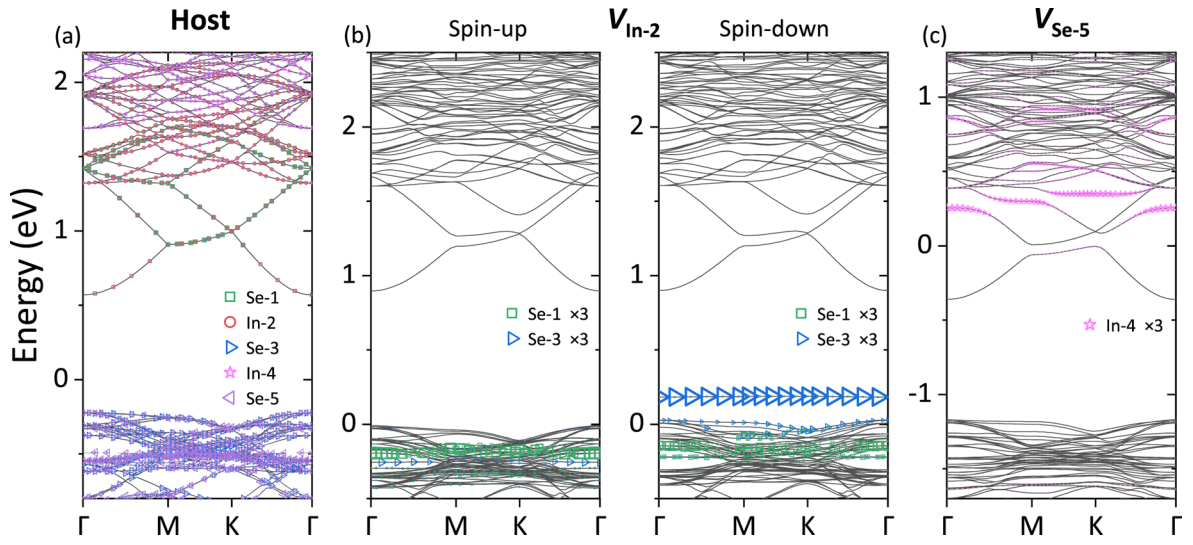

Figure 2. PBE band structures of (a) perfect α-In_2Se_3 and (b, c) the vacancy of In-2 and Se-5 in α-In_2Se_3, along with the projection of the sum of the contribution (to the energy bands) of the bond-breaking atoms around the defect. The size of the symbols represents the proportion of the atomic contribution. For a clear observation of defect states, the size of their symbols is enlarged by a factor of 3. The Fermi level is set to 0 eV.

thermodynamic transition levels of (0/−1) and (+1/0) within the bandgap, respectively. Meanwhile, V_{Se-1}, V_{In-2}, and V_{In-4} demonstrate both (0/−1) and (+1/0) transition levels within the bandgap. For these three defects, the energy difference between the (+1/0) level and conduction band minimum (CBM) is greater than the energy difference between the (0/−1) level and the valence band maximum (VBM), indicating that these defects predominantly act as acceptor-type defects.

The shallowest donor and acceptor defects are V_{Se-5} and V_{In-2} with ionization energies of 0.21 and 0.25 eV, respectively. Despite these ionization energies being significantly higher than the thermal energy at room temperature, they remain promising for contributing to the conductivity of 2D α-In_2Se_3 via defect-bound band edge states.[39] Figure 2 displays the projected band structures of pristine α-In_2Se_3 alongside In_2Se_3 with V_{In-2} and V_{Se-5}. The band structures of other defects are shown in the SI (Figure S1). In Figure 2(a), the proportions of the contributions to the bands are projected individually for each of the five sublayers, where the valence band is contributed mainly by Se-3 and Se-5 atoms, and the conduction band is primarily contributed by Se-1 and In-2 atoms.[40] The charge density distributions of the defect states are also provided in Figure S2 to help confirm the specific atoms contributing to these states. Compared with the band structure of pristine In_2Se_3, the removal of the bottom-layer selenium atom (V_{Se-5}) creates a defect level within the conduction band. Electrons occupying this defect level can spontaneously transfer to the lowest conduction band with no energy cost, as evidenced by the fact that the lowest conduction band is lower than the Fermi level in Figure 2(c). Due to the weakened screening, the electron is bound by the positively charged V_{Se-5}^{+} defect despite reaching the lowest conduction band, as evidenced by the corresponding charge density plot shown in Figure S3, which demonstrates the localization of the electron. Although these electrons are not free carriers, the occupied lowest conduction band, termed the defect-bound band-edge (DBBE) state, is reported to be able to facilitate carrier transport through wave function overlap at optimal doping densities.[39] In the DBBE state, the ionization energy can be described as $IE_0 = IE_i + E_{db}$, where IE_i corresponds to the energy required to ionize the defect state to the band edge, specifically, the conduction band minimum or the valence band maximum. The term E_{db} accounts for the additional energy necessary to overcome the exciton-like binding energy, enabling the formation of free carriers. For V_{Se-5}, the defect level is above the conduction band edge with IE_i = 0 eV, and since the calculated ionization energy IE_0 is 0.21 eV, $E_{db} = IE_0 - IE_i$ = 0.21 eV. Similarly, we also identified the DBBE state in the system with V_{In-2}, where the highest valence band in the spin-down channel is partially occupied, indicating the presence of a hole bound by the negatively charged V_{In-2}^{-}, as depicted in Figure 2(b). In terms of binding energy magnitude, V_{In-2} and V_{Se-5} in the monolayer of In_2Se_3 are comparable to Re_{Mo} in a monolayer of MoS_2, which is known to be the source of *n*-type conductivity of MoS_2.[39] This implies that V_{Se-5} could be responsible for the observed *n*-type conductivity in α-In_2Se_3, while V_{In-2} emerges as a promising candidate for the *p*-type defect. In the band structures of other defects (Figure S1), V_{Se-1} and V_{Se-3} are deep-level defects, while V_{In-4} is a shallow acceptor defect but with a larger formation energy than V_{In-2}.

We also found that V_{Se-3}, the most energetically preferred vacancy defect in α-In_2Se_3, can enhance the ferroelectric stability of the material. Figures 3(a), 3(c), and S4(a)−(d) demonstrate that the pristine ferroelectric α-phase rapidly converts to the paraelectric β-phase within the first 5 ps of a total 20 ps simulation at 750 K, which is consistent with findings reported about the rapid phase transition of defect-free systems in the literature.[41] The atomic displacements in the *x* and *y* directions indicate that the upper two layers and the lower three layers move in opposite directions, demonstrating that the α-to-β transition is driven by a highly coordinated movement among these atomic layers. This observation aligns with previous research suggesting that such atomic motion is linked to shear phonon mode.[42] In contrast, the presence of the V_{Se-3} defect introduces local structural distortions, which interfere with the uniform slipping of atomic layers, thus decelerating the α-to-β transition to 9 ps, as depicted in Figures 3(b), 3(d), and S4(e)−(h). A similar deceleration effect is also observed in the system containing

https://doi.org/10.1021/acs.nanolett.4c05165
Nano Lett. XXXX, XXX, XXX−XXX

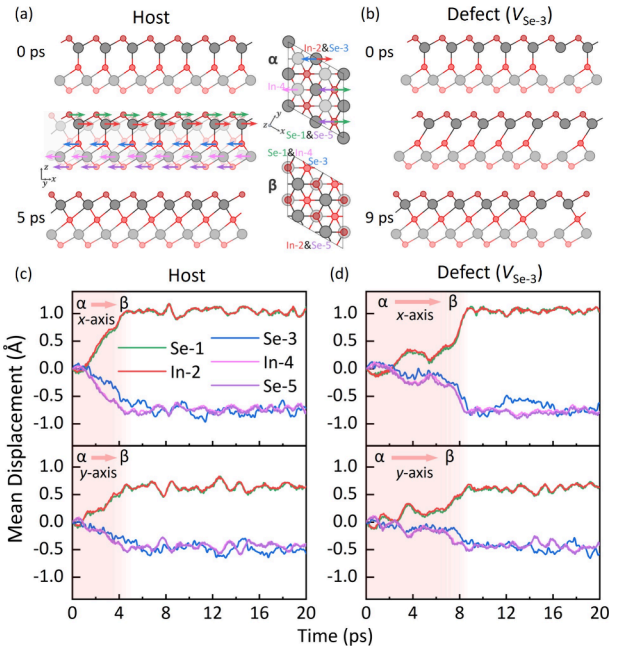

Figure 3. Molecular dynamics simulations of the ferroelectric-to-paraelectric (α-to-β) phase transition of 2D In_2Se_3. (a) Schematic illustrations (the side view) of the initial, superimposed, and final states of the transition in the perfect system (without defects) and the top view of the phase transition process. (b) Schematic diagram of the initial, intermediate, and final states in the system with a V_{Se-3} defect. (c) and (d) show the atomic displacements of perfect and defective 2D In_2Se_3, respectively, along the x- and y-axis during the transition.

another vacancy defect such as V_{Se-5}, as shown in Figure S5. The presence of V_{Se-5} results in the phase transition being delayed to around 18 ps. This finding suggests that such a vacancy defect disrupts the shear phonon mode critical for the phase transition, ultimately slowing the transition rate and enhancing the stability of the ferroelectric state.

To bridge the gap between theoretical predictions and experimental validations, we simulated the STM images of the five vacancy defects, as shown in Figures 4(a)−(j). Considering that α-In_2Se_3 has a quintuple-sublayer structure, we simulated the STM images for vacancies in the first three atomic layers from the top-down direction and for vacancies in the bottom three atomic layers from the bottom-up direction (the middle third layer is simulated from both perspectives).[43] At the same bias voltage, the bright and dark spots in the STM images of the perfect system appear similar in style from both the top view and the bottom view [VBM comparison in Figures 4(a) and 4(f), CBM comparison in Figures 4(e) and 4(j)], with only slight differences in shape due to the overlap of the positions of Se-1 and Se-5 in the x and y directions. For defective systems, the STM images can be linked to the defect states of the corresponding systems so that even though α-In_2Se_3 is not a single-atom-layer material, the STM images corresponding to vacancies in different layers can still be distinguished. For example, for V_{Se-1}, the impurity state is close to the CBM, with its band structures shown in Figure S1(a), while for V_{In-2} and V_{Se-3}, the impurity state is near the VBM, with their band structures shown in Figures 2(b) and S1(b), respectively. Therefore, under a positive bias voltage, V_{Se-1} is relatively easier to observe in the STM image in Figure 4(d), while V_{In-2} and V_{Se-3} are more easily observed under a negative bias voltage, as shown in Figures 4(b) and 4(c). For the most easily formed V_{Se-3}, compared to the top view [Figure 4(c)], the STM image contains more information about the host In_2Se_3 when viewed from the bottom [Figure 4(g)] because the Se-5 atoms contribute more in the VBM of the perfect system than Se-1 atoms do. For the source of n-type conductivity (V_{Se-5}) in Figure 4(i), since the Fermi level enters the conduction band, a smaller bias can be used to clearly observe the contribution of the defect. As an acceptor defect, V_{In-4} also exhibits significant brightness differences in the STM image [Figure 4(h)], which will be easily identifiable. We expect that the effort of STM analyses can help to identify the critical defects in 2D α-In_2Se_3 in future experiments.

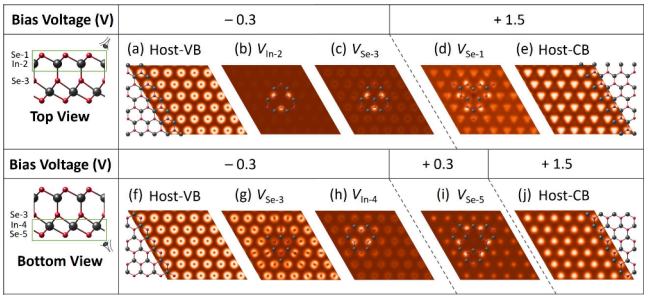

Figure 4. Simulated STM images of perfect and defective α-In_2Se_3 with constant-height mode. (a−e) Top-view STM images of perfect α-In_2Se_3 and that with defects. The overlaid atomic structure models on the STM images include the top two atomic layers, as the STM can more easily reveal the electron distribution of up to two surface atomic layers. (f−j) Bottom-view STM images of perfect α-In_2Se_3 and that with defects. The overlaid atomic structure models on the STM images include the bottom two atomic layers.

Leveraging experimental evidence that a vertical electric field can induce polarization reversal in α-In_2Se_3,[44] and inspired by our computational insights revealing polarization-defect coupling effect, where V_{Se-1} acts as a deep-level acceptor defect with downward polarization and V_{Se-5} as a shallow-level donor defect with upward polarization, here we propose a ferroelectric-controlled field-effect transistor based on 2D α-In_2Se_3 with defect engineering. As illustrated in Figure 5(a), α-In_2Se_3 with the V_{Se-5} defect under upward polarization is used as the electronic channel material, and the device initially operates in a low resistance state due to easily forming n-type conductivity by V_{Se-5}. When the gate bias shifts from positive to negative, the polarization of the channel material will change from upward to downward with an interesting result of V_{Se-5} simultaneously transitioning to V_{Se-1} and the device moving to a high resistance state due to the deep defect level of V_{Se-1}. Similarly, when the channel material containing the V_{Se-5} defect presents downward polarization, a change in bias direction can simultaneously switch its polarization direction and induce a transformation in its defect structure to V_{Se-1}, thereby facilitating the transition between low and high resistance states in the device, as shown in Figures 5(c) and (d). The polarization-induced transition from V_{Se-5} to V_{Se-1} in α-In_2Se_3 significantly reduces the carrier concentration due to the weak ionization of V_{Se-1} and the negligible hole conductivity, resulting in a substantial increase in resistance. We also calculated the CI-NEB barrier for domain wall motion in perfect and defective α-In_2Se_3 9 × 5 × 1 supercells to evaluate the effect of defects on ferroelectric polarization switching, as shown in Figure S6. This result indicates that while defects can locally increase the switching barrier, their impact on the

https://doi.org/10.1021/acs.nanolett.4c05165
Nano Lett. XXXX, XXX, XXX−XXX

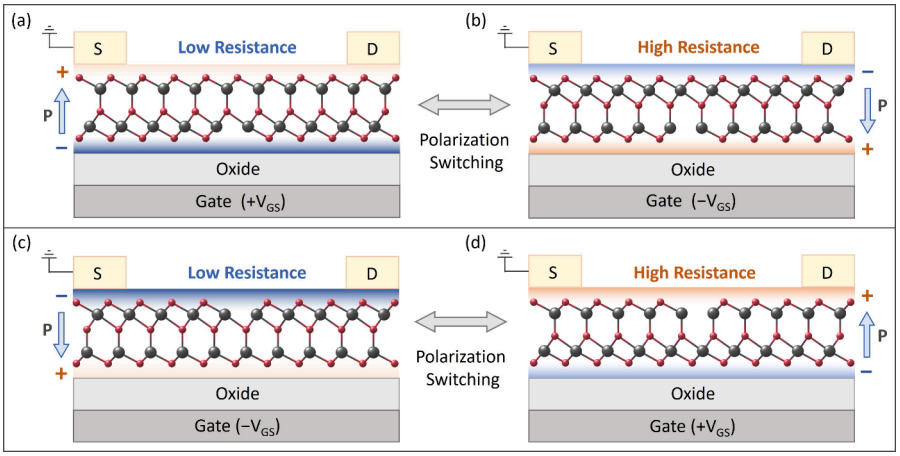

Figure 5. A new strategy of defect-engineered ferroelectric field-effect transistor based on α-In_2Se_3. (a) $V_{Se\text{-}5}$ defect with upward polarization, corresponding to the low resistance state under positive gate voltage. (b) $V_{Se\text{-}1}$ defect (changed from a $V_{Se\text{-}5}$ defect after polarization switching) with downward polarization, corresponding to a high resistance state under negative gate voltage. (c) $V_{Se\text{-}5}$ defect with downward polarization, corresponding to a low resistance state under negative gate voltage. (d) $V_{Se\text{-}1}$ defect (changed from a $V_{Se\text{-}5}$ defect after polarization switching) with upward polarization, corresponding to a high resistance state under positive gate voltage.

macroscopic switching behavior of the system is relatively limited. To investigate the potential effects of unintentional defects on the device design, we analyzed the band structures of a monolayer α-In_2Se_3 system containing both $V_{Se\text{-}5}$ and $V_{Se\text{-}3}$ defects, as $V_{Se\text{-}3}$ is the most likely to form according to formation energy calculations. The results, as shown in Figure S7, indicate that the band structure of this double defect system closely resembles that of a system containing only $V_{Se\text{-}5}$, suggesting that the presence of unintended defects, like $V_{Se\text{-}3}$, may have little impact on the performance of the proposed device. Note that here the resistance change induced by polarization switching does not imply a change in carrier type, since the high ionization energy of $V_{Se\text{-}1}$ makes the observation of *p*-type (hole) carriers less likely. This capability is particularly significant in applications such as data storage, where the ability to switch between different resistance states enables nonvolatile memory function, or in logic circuits where such switching enhances the efficiency of digital computing.

In summary, we have systematically investigated the properties of vacancy defects in monolayer ferroelectric α-In_2Se_3. Using the WLZ method, we established that when α-In_2Se_3 is polarized upward, the bottom-layer selenium vacancy ($V_{Se\text{-}5}$) possesses a donor ionization energy as small as 0.21 eV, which could potentially account for the origin of *n*-type conductivity experimentally observed in α-In_2Se_3 through defect-bound band-edge states. Similarly, the second-layer indium vacancy ($V_{In\text{-}2}$) emerged as a promising candidate for *p*-type doping, with an ionization energy of 0.25 eV. Furthermore, the middle-layer selenium vacancy ($V_{Se\text{-}3}$), the most readily formed defect, significantly bolsters the ferroelectric stability of α-In_2Se_3 by decelerating the phase transition to paraelectric β-In_2Se_3. We also provided simulated STM images of all defects to facilitate further experimental verification. Finally, we proposed a ferroelectric-controlled field-effect transistor based on α-In_2Se_3 that modulates the resistance state through alterations in polarization direction and defect configuration. This study significantly deepens our understanding of the polarization-defect coupling effects in 2D α-In_2Se_3, while also presenting innovative approaches for leveraging defect engineering in the design of advanced electronic and memory devices at the nanoscale.

■ ASSOCIATED CONTENT

Supporting Information

The Supporting Information is available free of charge at https://pubs.acs.org/doi/10.1021/acs.nanolett.4c05165.

Formation energy and ionization energy of defect in materials; the WLZ method for defects in 2D materials; band structure of 2D α-In_2Se_3 with vacancy; charge distribution of defect states and defect-bound band edge states; MD simulation of phase transition from α-In_2Se_3 to β-In_2Se_3; polarization switching barrier in perfect and defective α-In_2Se_3; energy bands of $V_{Se\text{-}5}$ and $V_{Se\text{-}5}$+$V_{Se\text{-}3}$; resistance estimation of $V_{Se\text{-}5}$ and $V_{Se\text{-}1}$ systems in FeS-FET devices (PDF)

■ AUTHOR INFORMATION

Corresponding Authors

Dan Wang − *School of Materials Science and Engineering, Beijing Institute of Technology, Beijing 100081, China*; Email: dan.wang@bit.edu.cn

Yu-Ting Huang − *State Key Laboratory of Integrated Optoelectronics, College of Electronic Science and Engineering, Jilin University, Changchun 130012, China*; orcid.org/0009-0005-9208-2780; Email: huangyuting@jlu.edu.cn

Nian-Ke Chen − *State Key Laboratory of Integrated Optoelectronics, College of Electronic Science and Engineering, Jilin University, Changchun 130012, China*; Email: chennianke@jlu.edu.cn

Xian-Bin Li − *State Key Laboratory of Integrated Optoelectronics, College of Electronic Science and Engineering, Jilin University, Changchun 130012, China*; orcid.org/0000-0002-0046-2016; Email: lixianbin@jlu.edu.cn

Authors

Ming-Yu Ma − *State Key Laboratory of Integrated Optoelectronics, College of Electronic Science and Engineering, Jilin University, Changchun 130012, China*

Dong Han − *College of Information Science and Engineering, Northeastern University, Shenyang 110819, People's Republic of China; State Key Laboratory of Luminescence Science and Technology, Changchun Institute of Optics, Fine Mechanics*

https://doi.org/10.1021/acs.nanolett.4c05165
Nano Lett. XXXX, XXX, XXX−XXX

and Physics, Chinese Academy of Sciences, Changchun 130033, People's Republic of China

Hong-Bo Sun − *State Key Laboratory of Precision Measurement Technology and Instruments, Department of Precision Instrument, Tsinghua University, Beijing 100084, China;* orcid.org/0000-0003-2127-8610

Shengbai Zhang − *Department of Physics, Applied Physics, and Astronomy, Rensselaer Polytechnic Institute, Troy, New York 12180, United States*

Complete contact information is available at: https://pubs.acs.org/10.1021/acs.nanolett.4c05165

Notes

The authors declare no competing financial interest.

■ ACKNOWLEDGMENTS

Work in China was supported by the National Science and Technology Major Project (grant no. 2022ZD0117600), the National Natural Science Foundation of China (grants nos. 12274172, 12304098, 12274180, 12474079), China Postdoctoral Science Foundation (grant no. BX20240136), the Science and Technology Development Plan Project of Jilin Province, China (grant no. 20230101004JC), and the Open Fund of the State Key Laboratory of Luminescence Science and Technology (grant no. SKLA-2024-01). The High-Performance Computing Center (HPCC) at Jilin University for computational resources is also acknowledged.

■ REFERENCES

(1) Liu, K.; Zhang, T.; Dang, B.; Bao, L.; Xu, L.; Cheng, C.; Yang, Z.; Huang, R.; Yang, Y. An Optoelectronic Synapse Based on α-In_2Se_3 with Controllable Temporal Dynamics for Multimode and Multiscale Reservoir Computing. *Nat. Electron.* **2022**, *5* (11), 761−773.

(2) Xin, C.; Yin, Y.; Song, B.; Fan, Z.; Song, Y.; Pan, F. Machine Learning-Accelerated Discovery of Novel 2D Ferromagnetic Materials with Strong Magnetization. *Chip* **2023**, *2* (4), 100071.

(3) Huang, Y.-T.; Li, Z.-Z.; Chen, N.-K.; Wang, Y.; Sun, H.-B.; Zhang, S.; Li, X.-B. Complex Charge Density Waves in Simple Electronic Systems of Two-Dimensional III_2-VI_3 Materials. *Nat. Commun.* **2024**, *15* (1), 9983.

(4) Wang, Z.; Zhou, X.; Liu, X.; Qiu, A.; Gao, C.; Yuan, Y.; Jing, Y.; Zhang, D.; Li, W.; Luo, H.; Chu, J.; Sun, J. Van Der Waals Ferroelectric Transistors: The All-Round Artificial Synapses for High-Precision Neuromorphic Computing. *Chip* **2023**, *2* (2), 100044.

(5) Xue, H.; Peng, Y.; Jing, Q.; Zhou, J.; Han, G.; Fu, W. Sensing with Extended Gate Negative Capacitance Ferroelectric Field-Effect Transistors. *Chip* **2024**, *3* (1), 100074.

(6) Ding, W.; Zhu, J.; Wang, Z.; Gao, Y.; Xiao, D.; Gu, Y.; Zhang, Z.; Zhu, W. Prediction of Intrinsic Two-Dimensional Ferroelectrics in In_2Se_3 and Other III_2-VI_3 van Der Waals Materials. *Nat. Commun.* **2017**, *8* (1), 14956.

(7) Huang, Y.-T.; Chen, N.-K.; Li, Z.-Z.; Wang, X.-P.; Sun, H.-B.; Zhang, S.; Li, X.-B. Two-dimensional In_2Se_3: A Rising Advanced Material for Ferroelectric Data Storage. *InfoMat* **2022**, *4*, e12341 DOI: 10.1002/inf2.12341.

(8) Si, M.; Saha, A. K.; Gao, S.; Qiu, G.; Qin, J.; Duan, Y.; Jian, J.; Niu, C.; Wang, H.; Wu, W.; Gupta, S. K.; Ye, P. D. A Ferroelectric Semiconductor Field-Effect Transistor. *Nat. Electron.* **2019**, *2* (12), 580−586.

(9) Zhang, J.; Zhang, X.; Wang, Y.; Cheng, P.; Feng, B.; Wu, K.; Lu, Y.; Chen, L. Giant Bandgap Engineering in Two-Dimensional Ferroelectric α-In_2Se_3. *J. Phys. Chem. Lett.* **2022**, *13* (14), 3261−3268.

(10) Tang, W.; Zhang, X.; Yu, H.; Gao, L.; Zhang, Q.; Wei, X.; Hong, M.; Gu, L.; Liao, Q.; Kang, Z.; Zhang, Z.; Zhang, Y. A van Der Waals Ferroelectric Tunnel Junction for Ultrahigh-Temperature Operation Memory. *Small Methods* **2022**, *6* (4), 2101583.

(11) Liu, Z.; Hou, P.; Sun, L.; Tsymbal, E. Y.; Jiang, J.; Yang, Q. In-Plane Ferroelectric Tunnel Junctions Based on 2D α-In_2Se_3/Semiconductor Heterostructures. *npj Comput. Mater.* **2023**, *9* (1), 6.

(12) Wan, S.; Li, Y.; Li, W.; Mao, X.; Wang, C.; Chen, C.; Dong, J.; Nie, A.; Xiang, J.; Liu, Z.; Zhu, W.; Zeng, H. Nonvolatile Ferroelectric Memory Effect in Ultrathin α-In_2Se_3. *Adv. Funct. Mater.* **2019**, *29* (20), 1808606.

(13) Wang, X.; Feng, Z.; Cai, J.; Tong, H.; Miao, X. All-van Der Waals Stacking Ferroelectric Field-Effect Transistor Based on In_2Se_3 for High-Density Memory. *Sci. China Inf. Sci.* **2023**, *66* (8), 182401.

(14) Wang, L.; Wang, X.; Zhang, Y.; Li, R.; Ma, T.; Leng, K.; Chen, Z.; Abdelwahab, I.; Loh, K. P. Exploring Ferroelectric Switching in α-In_2Se_3 for Neuromorphic Computing. *Adv. Funct. Mater.* **2020**, *30* (45), 2004609.

(15) Baek, S.; Yoo, H. H.; Ju, J. H.; Sriboriboon, P.; Singh, P.; Niu, J.; Park, J.-H.; Shin, C.; Kim, Y.; Lee, S. Ferroelectric Field-Effect-Transistor Integrated with Ferroelectrics Heterostructure. *Adv. Sci.* **2022**, *9* (21), 2200566.

(16) Wang, S.; Liu, L.; Gan, L.; Chen, H.; Hou, X.; Ding, Y.; Ma, S.; Zhang, D. W.; Zhou, P. Two-Dimensional Ferroelectric Channel Transistors Integrating Ultra-Fast Memory and Neural Computing. *Nat. Commun.* **2021**, *12* (1), 53.

(17) Zeng, J.; Feng, G.; Wu, G.; Liu, J.; Zhao, Q.; Wang, H.; Wu, S.; Wang, X.; Chen, Y.; Han, S.; Tian, B.; Duan, C.; Lin, T.; Ge, J.; Shen, H.; Meng, X.; Chu, J.; Wang, J. Multisensory Ferroelectric Semiconductor Synapse for Neuromorphic Computing. *Adv. Funct. Mater.* **2024**, *34*, 2313010.

(18) Nguyen, T. H.; Nguyen, V. Q.; Duong, A. T.; Cho, S. 2D Semiconducting α-In_2Se_3 Single Crystals: Growth and Huge Anisotropy during Transport. *J. Alloys Compd.* **2019**, *810*, 151968.

(19) Rodriguez, J. R.; Murray, W.; Fujisawa, K.; Lee, S. H.; Kotrick, A. L.; Chen, Y.; Mckee, N.; Lee, S.; Terrones, M.; Trolier-McKinstry, S.; Jackson, T. N.; Mao, Z.; Liu, Z.; Liu, Y. Electric Field Induced Metallic Behavior in Thin Crystals of Ferroelectric α-In_2Se_3. *Appl. Phys. Lett.* **2020**, *117* (5), 052901.

(20) Poh, S. M.; Tan, S. J. R.; Wang, H.; Song, P.; Abidi, I. H.; Zhao, X.; Dan, J.; Chen, J.; Luo, Z.; Pennycook, S. J.; Castro Neto, A. H.; Loh, K. P. Molecular-Beam Epitaxy of Two-Dimensional In_2Se_3 and Its Giant Electroresistance Switching in Ferroresistive Memory Junction. *Nano Lett.* **2018**, *18* (10), 6340−6346.

(21) Kremer, G.; Mahmoudi, A.; M'Foukh, A.; Bouaziz, M.; Rahimi, M.; Della Rocca, M. L.; Le Fèvre, P.; Dayen, J.-F.; Bertran, F.; Matzen, S.; Pala, M.; Chaste, J.; Oehler, F.; Ouerghi, A. Quantum Confinement and Electronic Structure at the Surface of van Der Waals Ferroelectric α-In_2Se_3. *ACS Nano* **2023**, *17*, 18924.

(22) Hou, P.; Wang, C.; Chen, Y.; Zhong, Q.; Zhang, Y.; Guo, H.; Zhong, X.; Wang, J.; Ouyang, X. Ionization Effect and Displacement Effect Induced Photoresponsivity Degradation on α-In_2Se_3 Based Transistors for Photodetectors. *Radiat. Phys. Chem.* **2020**, *174*, 108969.

(23) Hou, P.; Chen, Y.; Wang, X.; Lv, Y.; Guo, H.; Wang, J.; Zhong, X.; Ouyang, X. The Total Dose Effect of γ-Ray Induced Domain Evolution on α-In_2Se_3 Nanoflakes. *Phys. Chem. Chem. Phys.* **2020**, *22* (14), 7160−7164.

(24) Hou, P.; Wang, X.; Liu, Y.; Chen, Y.; Dong, S.; Guo, H.; Wang, J.; Zhong, X.; Ouyang, X. A Neutron Irradiation-Induced Displacement Damage of Indium Vacancies in α-In_2Se_3 Nanoflakes. *Phys. Chem. Chem. Phys.* **2020**, *22* (28), 15799−15804.

(25) Cai, C.; Hou, P.; Zhou, P.; Li, B. Strong Photodetection Enhancement of Quasi-2D Transistor through Defect Engineering. *Nucl. Instrum. Methods. Phys. Res. B* **2022**, *532*, 19−26.

(26) Tang, C.; Zhang, L.; Wijethunge, D.; Ostrikov, K. K.; Du, A. Controllable Polarization and Doping in Ferroelectric In_2Se_3 Monolayers and Heterobilayers via Intrinsic Defect Engineering. *J. Phys. Chem. C* **2021**, *125* (44), 24648−24654.

(27) Kresse, G.; Furthmüller, J. Efficiency of Ab-Initio Total Energy Calculations for Metals and Semiconductors Using a Plane-Wave Basis Set. *Comput. Mater. Sci.* **1996**, *6* (1), 15−50.

(28) Kresse, G.; Furthmüller, J. Efficient Iterative Schemes for *Ab Initio* Total-Energy Calculations Using a Plane-Wave Basis Set. *Phys. Rev. B* **1996**, *54* (16), 11169−11186.
(29) Perdew, J. P.; Burke, K.; Ernzerhof, M. Generalized Gradient Approximation Made Simple. *Phys. Rev. Lett.* **1996**, *77* (18), 3865−3868.
(30) Kresse, G.; Joubert, D. From Ultrasoft Pseudopotentials to the Projector Augmented-Wave Method. *Phys. Rev. B* **1999**, *59* (3), 1758−1775.
(31) Wang, D.; Han, D.; Li, X.-B.; Xie, S.-Y.; Chen, N.-K.; Tian, W. Q.; West, D.; Sun, H.-B.; Zhang, S. B. Determination of Formation and Ionization Energies of Charged Defects in Two-Dimensional Materials. *Phys. Rev. Lett.* **2015**, *114* (19), 196801.
(32) Wang, D.; Han, D.; Li, X.-B.; Chen, N.-K.; West, D.; Meunier, V.; Zhang, S.; Sun, H.-B. Charged Defects in Two-Dimensional Semiconductors of Arbitrary Thickness and Geometry: Formulation and Application to Few-Layer Black Phosphorus. *Phys. Rev. B* **2017**, *96* (15), 155424.
(33) Wang, V.; Xu, N.; Liu, J.-C.; Tang, G.; Geng, W.-T. VASPKIT: A User-Friendly Interface Facilitating High-Throughput Computing and Analysis Using VASP Code. *Comput. Phys. Commun.* **2021**, *267*, 108033.
(34) Nosé, S. A Unified Formulation of the Constant Temperature Molecular Dynamics Methods. *J. Chem. Phys.* **1984**, *81* (1), 511−519.
(35) Henkelman, G.; Uberuaga, B. P.; Jónsson, H. A Climbing Image Nudged Elastic Band Method for Finding Saddle Points and Minimum Energy Paths. *J. Chem. Phys.* **2000**, *113* (22), 9901−9904.
(36) KüPers, M.; Konze, P. M.; Meledin, A.; Mayer, J.; Englert, U.; Wuttig, M.; Dronskowski, R. Controlled Crystal Growth of Indium Selenide, In_2Se_3, and the Crystal Structures of α-In_2Se_3. *Inorg. Chem.* **2018**, *57* (18), 11775−11781.
(37) Han, W.; Zheng, X.; Yang, K.; Tsang, C. S.; Zheng, F.; Wong, L. W.; Lai, K. H.; Yang, T.; Wei, Q.; Li, M.; Io, W. F.; Guo, F.; Cai, Y.; Wang, N.; Hao, J.; Lau, S. P.; Lee, C.-S.; Ly, T. H.; Yang, M.; Zhao, J. Phase-Controllable Large-Area Two-Dimensional In_2Se_3 and Ferroelectric Heterophase Junction. *Nat. Nanotechnol.* **2023**, *18* (1), 55−63.
(38) Huang, M.; Cai, Z.; Wang, S.; Gong, X.; Wei, S.; Chen, S. More Se Vacancies in Sb_2Se_3 under Se-Rich Conditions: An Abnormal Behavior Induced by Defect-Correlation in Compensated Compound Semiconductors. *Small* **2021**, *17* (36), 2102429.
(39) Wang, D.; Han, D.; West, D.; Chen, N.-K.; Xie, S.-Y.; Tian, W. Q.; Meunier, V.; Zhang, S.; Li, X.-B. Excitation to Defect-Bound Band Edge States in Two-Dimensional Semiconductors and Its Effect on Carrier Transport. *npj Comput. Mater.* **2019**, *5* (1), 8.
(40) Tao, S.; Zhang, X.; Zhu, J.; He, P.; Yang, S. A.; Lu, Y.; Wei, S.-H. Designing Ultra-Flat Bands in Twisted Bilayer Materials at Large Twist Angles: Theory and Application to Two-Dimensional Indium Selenide. *J. Am. Chem. Soc.* **2022**, *144* (9), 3949−3956.
(41) Liu, J.; Pantelides, S. T. Pyroelectric Response and Temperature-Induced α-β Phase Transitions in α-In_2Se_3 and Other α-III_2VI_3 (III = Al,Ga,In; VI = S,Se) Monolayers. *2d Mater.* **2019**, *6* (2), 025001.
(42) Huang, Y.-T.; Chen, N.-K.; Li, Z.-Z.; Li, X.-B.; Wang, X.-P.; Chen, Q.-D.; Sun, H.-B.; Zhang, S. Mexican-Hat Potential Energy Surface in Two-Dimensional III_2-VI_3 Materials and the Importance of Entropy Barrier in Ultrafast Reversible Ferroelectric Phase Change. *Appl. Phys. Rev.* **2021**, *8* (3), 031413.
(43) Han, D.; Li, X.-B.; Wang, D.; Chen, N.-K.; Fan, X.-W. Doping in the Two-Dimensional Limit: *P*/*n* -Type Defects in Monolayer ZnO. *Phys. Rev. B* **2022**, *105* (2), 024104.
(44) Xiao, J.; Zhu, H.; Wang, Y.; Feng, W.; Hu, Y.; Dasgupta, A.; Han, Y.; Wang, Y.; Muller, D. A.; Martin, L. W.; Hu, P.; Zhang, X. Intrinsic Two-Dimensional Ferroelectricity with Dipole Locking. *Phys. Rev. Lett.* **2018**, *120* (22), 227601.

https://doi.org/10.1021/acs.nanolett.4c05165
Nano Lett. XXXX, XXX, XXX−XXX